https://doi.org/10.1016/j.jsv.2023.117781

A Sonic Black Hole Structure with Perforated Boundary for Slow Wave Generation

Sihui Li[a], Jiajun Xia[a], Xiang Yu[a,*], Xiaoqi Zhang[b], Li Cheng[a,*]

[a] Department of Mechanical Engineering, The Hong Kong Polytechnic University, Kowloon, Hong Kong, China

[b] School of Naval Architecture, Ocean and Energy Power Engineering, Wuhan University of Technology, Wuhan 430063, China

* Corresponding author.

E-mail address: li.cheng@polyu.edu.hk (Li Cheng)

lucien.yu@polyu.edu.hk (Xiang Yu)

ABSTRACT

A Sonic Black Hole (SBH) in a retarding duct structure incorporates two indispensable physical processes, *i.e.*, wave energy focalization and dissipation, to entail slow-sound effect and broadband sound absorption. Original SBH design, however, involves a large number of inner rings inside the duct to produce the required impedance changes. In this study, a SBH configuration with perforated boundary (SBH-PB) is examined, in which perforated acoustic boundaries are used to achieve enhanced SBH effects. Upon a dedicated treatment of the perforated boundary (PB) with the backing cavity, the transfer matrix method (TMM) is adopted to analyze the acoustic characteristics of the SBH-PB and to explore the underlying physical mechanisms. The adoption of the PB is shown to bring about threefold benefits: increased accuracy of the TMM modeling owing to the weakened coupling among the backing cavities in the SBH-PB, enhanced sound absorption through micro-perforations, and the realization of SBH effects with a reduced number of inner rings. To visualize the slow-sound effect, the change of sound speed is examined through transient simulations using finite element method by capturing the wavefront propagation inside the duct. Finally, for the first time, an acoustic duct system replicating the transient simulations is developed to experimentally demonstrate the slow-wave phenomenon in the time domain. The proposed structure holds promises for sound wave manipulation and the development of acoustic noise control devices.

Keywords: Sonic Black Hole; perforated boundary; transfer matrix method; slow-sound metamaterial; transient analysis

A list of abbreviations and variables

Abbreviations

SBH	Sonic Black Hole
SBH-PB	Sonic Black Hole with Perforated Boundary
TMM	Transfer Matrix Method
FEM	Finite Element Method

Variables

R	the radius of the initial duct
$r(x)$	the inner radius of the rings at the position x
r	the minimum inner radius of the rings at the SBH-PB truncation
L	the total length of the SBH-PB structure
d	the distance between two adjacent rings
R_h, t, δ	the hole diameter, thickness and perforation rate of the perforated boundary
N	the number of discretized elements in SBH-PB structure
p_i, v_i	the sound pressure and particle velocity at the entry end in the i-th element
p_{i+1}, v_{i+1}	the sound pressure and particle velocity at the exit end in the i-th element
A_i, B_i	the amplitude of the incident and reflected waves of the i-th layer
k_0	the wave number
u_i, u_{i+1}	the volumetric velocity at the entry and exit end of the i-th element
$u_{\mathrm{PB}i}$	the volumetric velocity at the PB in the i-th element
ρ_0, c_0	the air density and velocity of sound wave in air
S_i, S_{i+1}	the inner ring areas at the entry and exit end of the i-th element
R_i, R_{i+1}	the radius of the inner rings at the entry and exit end in the i-th element
$p_{\mathrm{PB}i}, v_{\mathrm{PB}i}$	the sound pressure and particle velocity at the PB in the i-th element
Z_{ui}	the total surface impedance of PB and the air cavity behind in the i-th element
$S_{\mathrm{PB}i}$	the area of the surrounding PB in the i-th element
Z_{PB}, Z_{ci}	the surface impedance of the PB and the air cavity behind PB
$\boldsymbol{T_i}$	the transfer matrix between the state vector at the entry end and the state vector at the exit end in i-th element
$\boldsymbol{T_s}$	the total transfer matrix of the SBH-PB
R_c	the reflection coefficient of the SBH-PB
H_i, V_{ci}	the vertical height and the volume of the backing cavity
R_s	the surface resistance of the PB
ε_e	the correction length of the PB

1. Introduction

Sonic black hole (SBH), as a new type of sound wave manipulation means, is attracting increasing attention recently. Capitalizing on its salient features in terms of wave retarding and energy trapping, SBH offers a promising solution for low-frequency and broadband sound manipulation. The exploration of the phenomena is particularly useful to address the growing need for passive noise control and the development of acoustic wave manipulation devices.

The concept of the SBH falls into a border category of problems, generally referred to as Acoustic Black Hole (ABH), which has witnessed a flourished development during the last two decades [1, 2], predominantly for the manipulation of bending waves in solids. Inspired by the basic concept proposed by Pierre Simon Laplace in astrophysics and related research by Pekeris in acoustics [3], Mironov discovered that similar phenomena could be reproduced for bending waves in a wedge-shaped structure [4]. By tailoring the thickness of a beam, for example, according to a decreasing power-law relationship, the wave velocity of the incoming bending waves can be gradually deaccelerated to eventually entail wavelength compression and energy accumulation. In addition to the studies on the fundamental mechanisms and physical properties pertaining to structural ABH [5, 6], ABH concept has inspired novel structural design and the development of vibration control devices [7, 8]. In terms of modeling and analyses, various numerical methods have been proposed, including the Finite Element Method (FEM) [9], geometrical acoustic approach [10], Transfer Matrix Method (TMM) [11], Rayleigh-Ritz method [12] and energy-based semi-analytical method [13]. These methods allow for the analyses of the physical mechanisms of ABH as well as its geometric design and optimization. In addition, practical applications of ABH have also been explored, exemplified by lightweight and high damping structures [14], periodic lattices [15], vibration dampers [16] and energy harvesting devices [17], etc.

Comparatively, the counterpart of the structural ABH for acoustic waves, referred to as Sonic Black Hole (SBH), is much less explored despite a few exploratory research reported in the open literature. SBH exhibits similar ability in manipulating sound waves as compared with the structural ABH [4, 18]. Mironov first derived its basic theory and theoretically showed that a SBH structure with gradually varying admittance can decrease the speed of sound wave propagation to produce pronounced energy accumulation [18]. If the slow-sound effect is strong and smooth enough, the incident wave will not reach the end of the termination, resulting in zero wave reflection. Practically, the SBH effect can be achieved by installing a series of rings with a power-law decaying inner radius into a duct [19]. Several numerical modeling methods have been developed to model such systems, including semi-analytical method [20], TMM [21], and fractional order operators [22]. The acoustic performance of a SBH prototype has mostly been quantified by sound reflection coefficient calculated and measured in the frequency domain [23, 24]. Furthermore, the influence of some key parameters on the SBH performances, including the truncation length, number of rings, power-law profile, ring thickness, etc., have been discussed [21, 25, 26]. Meanwhile, some SBH-inspired retarding structures have also been investigated [27-29]. Despite these initial efforts, SBH for sound absorption was much less studied as compared with its structural counterpart. The associated physical mechanisms have not been fully understood.

SBH effect stems from a combination of wave retarding and energy dissipation processes.

Since air damping is usually weak, alternative damping treatment is necessary to enhance the energy dissipation and the overall SBH effect. In our previous research, a new SBH-inspired retarding structure was proposed as shown in Fig. 1, in which a perforated boundary (PB) was introduced as the liner inside a SBH duct. It was showed that, by adding perforated boundaries, SBH structure can offer broadband sound absorption. However, the analysis was performed through FEM. In addition to the heavy computational costs, the physical mechanisms underpinning the observed sound absorption performance were only explained in the frequency domain [30]. The numerous parameters involved in the system and the interplay among them call for more efficient modelling and analysis tools to be developed. Meanwhile, no convincing demonstration of the expected slow-sound phenomenon in the time domain was reported in the open literature. The addition of the perforated boundaries raises even more intriguing questions as to how the perforated boundaries could possibly affect the slow-wave phenomena and how they might impact the system design.

These issues motivate the present research, which shows its novelty by targeting a two-fold objective: 1) to establish an analytical TMM to simulate the SBH-PB structure with a proper treatment of the perforated boundary and define its validity range; 2) to explore the physical process underpinning the slow-wave phenomena in both frequency and time domains using both numerical and experimental means. The end outcome is to provide a general tool as well as the physical understanding to guide the design of effective SBH structures. More specifically, the paper is organized as follows. Section 2 first defines the basic SBH configuration and its geometric parameters. Then, a TMM model on SBH-PB structure is formulated. Note that although TMM has been previously employed to model conventional SBH structure, the equivalent version considering perforated boundaries as inner liners is not available, which forms one of the originalities of this paper. To this end, the impedance formula suitable for describing the acoustic characteristics of the added PB layer is developed. Section 3 validates the proposed TMM and verifies its improved accuracy as compared with the conventional SBH configuration. Advantages of the SBH-PB over the original form of SBH in terms of enhanced sound absorption and reduced structural complexity are also discussed. Finally, Section 4 further elaborates transient simulation and analysis alongside time-domain experiment to quantitatively describe the slow-sound phenomenon, which is not yet available up to now in the open literature.

2. Theory

2.1 SBH-PB model

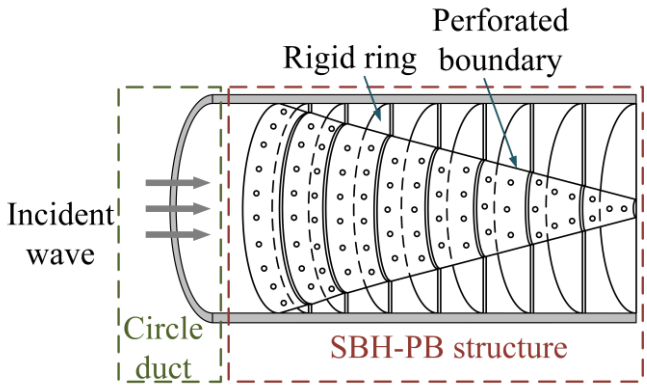

Fig. 1. Overall structure of the proposed SBH-PB model.

The basic SBH configuration as studied in [18] is used as the baseline to achieve the slow-sound effect, which consists of a series of rigid rings with a power-law decaying inner radius inside a duct. The damping from the inherent air frictional loss is weak. To achieve better energy dissipation, perforated boundary (PB) is embedded as the inner lining of the SBH, as schematically shown in Fig. 1. The SBH-PB is constructed to maximize the black hole effect through a simplified structural design (in terms of the number of required rings, to be demonstrated later) and to enhance the sound absorption. The PB separates the two acoustic fields (the inner side of the duct and the backing cavity between the ring partitions) which can only commute through the holes over the PB, which is assumed acoustically rigid without vibration. The key geometric parameters are marked in Fig. 2, where R represents the radius of the initial duct, as well as the maximum inner radius of the rings in the SBH-PB. The inner radius of the rings decreases according to a power-law function in the SBH-PB structure:

$$r(x) = \begin{cases} R & x < -L \\ \varepsilon x^m + r & -L < x < 0 \end{cases} \tag{1}$$

where x is the position along the waveguide direction. The SBH-PB structure is placed between $-L$ and 0. r is the minimum inner radius of the rings at the SBH-PB truncation (extreme right-side end). Ideally, the inner radius of the rings in the basic SBH configuration will be gradually decreased to 0. However, due to the practical manufacturing limitation, the SBH structure examined in this paper is truncated in the length direction with an inner radius of the ring r. L is the total length of the SBH-PB structure. d is the distance between two adjacent rings, which can be evenly or unevenly distributed. The figure also presents some essential parameters of the PB, including the hole diameter R_h and thickness of the plate t and the perforation rate δ. For sound absorption purposes, the SBH-PB retarding structure is placed at the termination end of a circular duct.

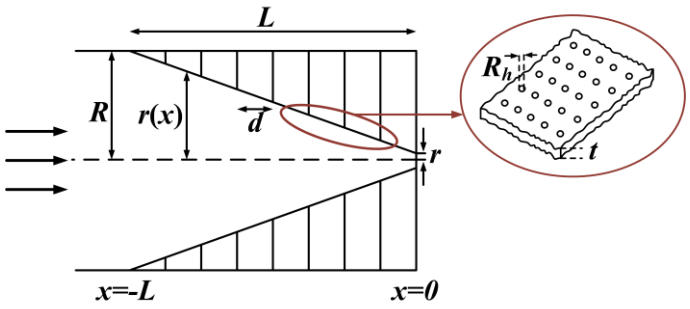

Fig. 2. Cross-section of the SBH system with inner perforated boundary facing showing the geometric variables.

2.2 TMM approach

TMM provides a fast and accurate method to model cascaded structures like the present SBH-PB. By assuming the sound wave propagations are primarily one-dimensional plane waves, TMM can provide a relatively accurate model to describe the behavior of realistic linear and quadratic retarding structures. As schematically shown in Fig. 3, the ring thickness is neglected, and each air cavity between the two adjacent rings is regarded as an element of the cascaded structure. This element consists of two subdomains, one corresponding to the air volume inside the shrinking duct, and the other to the outer air cavity, both being trapezoidal shaped in the cross-sectional drawing as shown in Fig. 3. In this way, the overall SBH-PB structure is discretized into N elements, which will be assembled through the continuity conditions established at the corresponding interfaces.

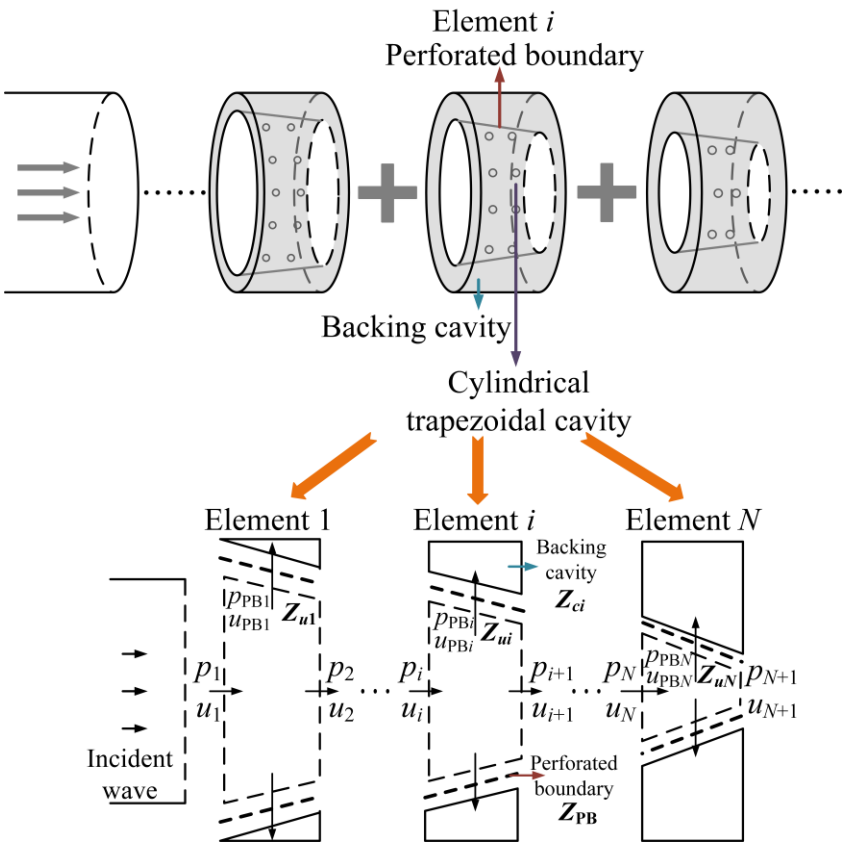

Fig. 3. TMM steps to model the proposed SBH-PB structure.

The TMM relates the state vectors of the acoustic pressures and particle velocities at the inlet and the outlet surfaces of a discretized layer. In the *i*-th element, as shown in Fig. 3, the state vector at the entry end $(p_i, v_i)^\tau$ and that at the exit end $(p_{i+1}, v_{i+1})^\tau$ can be connected by a transfer matrix. The coordinates of the entry end and the exit end are x_i and x_{i+1} respectively. For the acoustic pressure, using plane wave assumption in the inner duct (centered trapezoidal cavity of each element), the acoustic pressure p_i and p_{i+1} can be expressed as:

$$p_i = A_i e^{-jk_0 x_i} + B_i e^{+jk_0 x_i} \tag{2}$$

$$p_{i+1} = A_i e^{-jk_0 x_{i+1}} + B_i e^{+jk_0 x_{i+1}} \tag{3}$$

where A_i and B_i are the amplitudes of the incident and reflected waves of the *i*-th layer, respectively; j is the imaginary unit; k_0 is the wave number. Considering the change in the sectional area between the two ends, the volumetric velocity u_i can be expressed as

$$u_i = S_i v_i = S_i \frac{A_i e^{-jk_0 x_i} - B_i e^{+jk_0 x_i}}{\rho_0 c_0} \tag{4}$$

where v_i is the acoustic particle velocity; ρ_0 the air density; c_0 the velocity of sound wave in air; S_i the inner ring areas of the entry end. The outgoing velocity at the *i*-th element can be divided into two parts according to the mass conservation law. One part is the volumetric velocity at the exit end u_{i+1} of the *i*-th element flowing into the subsequent element, while the other part being the volumetric velocity at the PB u_{PBi} flowing into the outer cavity behind the PB. The continuity

condition of volumetric velocity writes:

$$u_{\mathrm{PB}i} + u_{i+1} = S_{i+1}\frac{A_i e^{-jk_0 x_{i+1}} - B_i e^{+jk_0 x_{i+1}}}{\rho_0 c_0} \tag{5}$$

where S_{i+1} is the inner ring area of the exit end.

The particle velocity at PB $v_{\mathrm{PB}i}$ can be simply expressed as the sound pressure at PB $p_{\mathrm{PB}i}$ divided by the surface impedance at PB Z_{ui} according to the definition. It writes

$$u_{\mathrm{PB}i} + u_{i+1} = S_{\mathrm{PB}i} v_{\mathrm{PB}i} + u_{i+1} = S_{\mathrm{PB}i}\frac{p_{\mathrm{PB}i}}{Z_{ui}} + u_{i+1} \tag{6}$$

where $S_{\mathrm{PB}i}$ is the area of the surrounding PB; Z_{ui} the total surface impedance of PB and the air cavity behind, which is described in detail in section 2.3. This term is the sum of the surface impedance of the air cavity behind PB Z_{ci} and the surface impedance of the PB itself Z_{PB}. Some approximations are applied during the derivation process. Specifically, considering the close distance between the two rings, d, the sound pressure at the surface of PB $p_{\mathrm{PB}i}$ can be approximated by using the sound pressure at the exit end p_{i+1}. This approximation has little effect on the results of TMM, and the detailed verification is omitted here. Therefore, Eq. (6) can also be expressed as

$$u_{\mathrm{PB}i} + u_{i+1} = S_{\mathrm{PB}i}\frac{p_{i+1}}{Z_{ci} + Z_{\mathrm{PB}}} + u_{i+1} \tag{7}$$

Importantly, the coordinates of the entry end and the exit end are x_i and x_{i+1} have such a relationship as $x_{i+1} = x_i + d$, where d is distance between two rings. Finally, according to the combination of all the previous formulas, we can obtain the final transfer matrix $\boldsymbol{T_i}$ between the state vector at the entry end $(p_i, v_i)^\tau$ and the state vector at the exit end $(p_{i+1}, v_{i+1})^\tau$ in *i*-th element as

$$\begin{bmatrix} p_i \\ u_i \end{bmatrix} = \boldsymbol{T_i}\begin{bmatrix} p_{i+1} \\ u_{i+1} \end{bmatrix} = \begin{bmatrix} cosk_0 d & j\frac{\rho_0 c_0}{S_{i+1}} sink_0 d \\ j\frac{S_i}{\rho_0 c_0} sink_0 d & cosk_0 d \end{bmatrix}\begin{bmatrix} 1 & 0 \\ \frac{S_{\mathrm{PB}i}}{Z_{ci} + Z_{\mathrm{PB}}} & 1 \end{bmatrix}\begin{bmatrix} p_{i+1} \\ u_{i+1} \end{bmatrix} \tag{8}$$

For the two adjacent elements, the exit end of the upstream element and the entry end of the downstream elements share the same surface, so the sound pressure and volume velocity of these two ends are represented by the same symbols. Therefore, using the transfer matrix $\boldsymbol{T_i}$ (*i*=1,2,3……) of each elements, the total transfer matrix $\boldsymbol{T_s}$ of the SBH-PB can also be obtained, by which the state vector $(p_1, u_1)^\tau$ at the beginning of the SBH-PB can be linked to those at the truncated end $(p_{N+1}, u_{N+1})^\tau$ (assuming the SBH-PB involves *N* elements, as shown in Fig. 3).

$$\begin{bmatrix} p_1 \\ u_1 \end{bmatrix} = \boldsymbol{T_s}\begin{bmatrix} p_{N+1} \\ u_{N+1} \end{bmatrix} = \boldsymbol{T_1 T_2} \ldots\ldots \boldsymbol{T_N}\begin{bmatrix} p_{N+1} \\ u_{N+1} \end{bmatrix} = \begin{bmatrix} T_{11} & T_{12} \\ T_{21} & T_{22} \end{bmatrix}\begin{bmatrix} p_{N+1} \\ u_{N+1} \end{bmatrix} \tag{9}$$

For the SBH-PB in one-dimensional duct, plane wave incidence is applied at the entrance. When the SBH-PB is terminated with a rigid end ($u_{N+1} = 0$), the reflection coefficient R_c can be

solved as

$$R_c = \left(\frac{zT_{11} - T_{21}}{T_{21} + zT_{11}}\right)^2 \tag{10}$$

where $z = \frac{S_1}{\rho_0 C_0}$, with S_1 being the cross-sectional area at the start of the SBH-PB. Note that the plane wave assumption requires the analysis frequency to be lower than the cut-off frequency of the incident duct:

$$f \leq 0.29 c_0 / R \tag{11}$$

where R denotes the radius of the duct.

3.3 Surface impedance of the PB

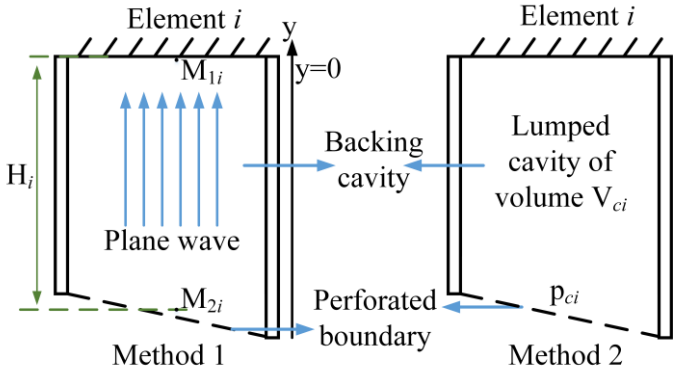

Fig. 4. Schematic diagram of two processing methods for the backing air cavity.

The accuracy of the TMM is significantly affected by the validity and the accuracy of the surface impedance Z_{ui}, estimated on the inner surface of the PB. Z_{ui} can be divided into two parts, the surface impedance of the air cavity behind PB, Z_{ci}, and the surface impedance of the PB itself Z_{PB}. The first part Z_{ci} can be calculated using two proposed methods, as depicted in Fig. 4. The first method is based on one-dimensional plane wave description of the outer cavity. In the backing cavity of the i-th element, the surface impedance Z_{1i} at Point M_{1i} and the surface impedance Z_{2i} at Point M_{2i} can be written as:

$$Z_{1i} = Z_0 \frac{C_i e^{-jk_0 y_{1i}} + D_i e^{+jk_0 y_{1i}}}{C_i e^{-jk_0 y_{1i}} - D_i e^{+jk_0 y_{1i}}} \tag{12}$$

$$Z_{2i} = Z_0 \frac{C_i e^{-jk_0 y_{2i}} + D_i e^{+jk_0 y_{2i}}}{C_i e^{-jk_0 y_{2i}} - D_i e^{+jk_0 y_{2i}}} \tag{13}$$

where C_i and D_i are the amplitudes of the incident and the reflected waves, respectively; y_{1i} and y_{2i} the coordinates of point M_{1i} and M_{2i}, respectively; Z_0 the characteristic impedance of air. Additionally, $y_{2i} = y_{1i} - H_i$ with H_i being the vertical height of the backing cavity, selected as the mean value or at the midpoint. Therefore, the relationship between Z_{1i} and Z_{2i} writes

$$Z_{2i} = Z_0 \frac{-jZ_{1i}\cot(k_0 H_i) + Z_0}{Z_{1i} - jZ_0 \cot(k_0 H_i)} \tag{14}$$

Because Point M_{1i} is near the rigid surface of the duct, $Z_{1i} \to \infty$, the surface impedance Z_{ci} of the air cavity can be reduced to:

$$Z_{ci} = Z_{2i} = -jZ_0 \cot(k_0 H_i) \tag{15}$$

The second method is to treat the air cavity as a lumped volume V_{ci}. In the backing cavity of the i-th element, applying an acoustic pressure p_{ci} at the surface of the air cavity as shown in Fig. 4, and letting the volume decrease by ΔV adiabatically, one has,

$$\frac{p_{ci}}{p_0} + \gamma \frac{\Delta V}{V_{ci}} = 0 \tag{16}$$

where γ is the volume expansion coefficient; p_0 the initial pressure. Then,

$$\Delta V = -\frac{S_{\mathrm{PB}i} v_{\mathrm{PB}i}}{j\omega} \tag{17}$$

where ω is the angular velocity. Then substituting Eq. (17) into Eq. (16) leads to the formula for the calculation of the acoustic pressure p_{ci}. According to the definition of the surface impedance, Z_{ci} writes

$$Z_{ci} = \frac{p_{ci}}{v_{\mathrm{PB}i}} = \frac{c_0^2 \rho_0 S_{\mathrm{PB}i}}{jwV_{ci}} \tag{18}$$

where V_{ci} is the volume of the air cavity which can be taken as a truncated cone,

$$V_{ci} = \pi d \left[R^2 - \frac{1}{3}(R_{i+1}^2 + R_i^2 + R_{i+1}R_i) \right] \tag{19}$$

where R is the radius of the duct; R_i and R_{i+1} are the radius of the inner rings at both ends of the element.

The choice of the applicable model for the second part Z_{PB} is very important, which necessities the consideration of the range of various parameters of the PB. For perforation hole sizes in the submillimeter range, Maa's micro-perforated plate model is usually adopted to calculate the surface impedance as [31]:

$$Z_{\mathrm{PB-Maa}} = Z_r + jZ_i \tag{20}$$

where

$$Z_r = \frac{32\eta t}{\delta R_h^2} k_r, k_r = \left[1 + \frac{k^2}{32} \right]^{\frac{1}{2}} + \frac{\sqrt{2}}{32} k \frac{R_h}{t} \tag{21}$$

$$Z_i = \frac{\omega t \rho_0}{\delta} k_i, k_i = 1 + \left[1 + \frac{k^2}{2} \right]^{-\frac{1}{2}} + 0.85 \frac{R_h}{t} \tag{22}$$

and

$$k = R_h \sqrt{\frac{\omega \rho_0}{4\eta}} \tag{23}$$

In which η is the coefficient of viscosity; t the thickness of the PB; δ the perforated rate and R_h the orifice diameter. For perforation with larger hole sizes, Allard Ingard's model can be used to calculate the surface impedance as [32]:

$$Z_{\mathrm{PB-AI}} = \left(\frac{4t}{R_h} + 4\right)\frac{R_s}{\delta} + \frac{j\rho_0\omega}{\delta}(2\varepsilon_{e-\mathrm{AI}} + t) \tag{24}$$

where

$$\varepsilon_{e-\mathrm{AI}} = 0.48\sqrt{\pi\left(\frac{R_h}{2}\right)^2}\left(1 - 1.14\sqrt{\delta}\right) \tag{25}$$

and

$$R_s = \frac{1}{2}\sqrt{2\eta\omega\rho_0} \tag{26}$$

To deal with a PB with variable ranges of perforation parameters, it is however cumbersome to divide the perforation diameters into two ranges, which will hamper the subsequent optimization of the hole parameters using a unified model. To solve this problem, we propose to employ Beranek Ingard's model to calculate the surface impedance of the PB [32]:

$$Z_{\mathrm{PB-BI}} = \left(\frac{4t}{R_h} + 4\right)\frac{R_s}{\delta} + j\frac{\omega\rho_0}{\delta}(2\varepsilon_{e-\mathrm{BI}} + t) + j\left(\frac{4t}{R_h} + 4\right) \tag{27}$$

where

$$\varepsilon_{e-\mathrm{BI}} = 0.48\sqrt{\pi\left(\frac{R_h}{2}\right)^2}\left(1 - 1.47\sqrt{\delta} + 0.47\sqrt{\delta^3}\right) \tag{28}$$

where R_s denotes the surface resistance; ε_e represents a correction length, which is a function of the perforation ratio together with the hole diameter. The real part of the surface impedance is the acoustic resistance which is associated with the acoustic energy dissipation due to viscous effects. The imaginary part is referred to as the acoustic reactance, which represents the inertial effects. The applicability and suitability of the proposed modeling method will be verified both numerically and experimentally in accordance with the PB with different parameter ranges.

3. Frequency domain analyses and experimental validation

3.1 Validation of the TMM against FEM

The proposed PB modeling method is first assessed. According to the applicable range of the impedance models, Maa's model is usually used to model the micro-perforated plate, while Allard Ingard's model is applied for the perforated plate with larger hole size. To verify whether Beranek Ingard's model is suitable for modeling PB with varying hole diameters, two configurations of PB structures are tested, whose parameters are given in Table 1. Both PBs (PB 1 and PB 2) have the same thickness t and perforation ratio δ, but with different hole diameters. PB 1 has a smaller hole diameter in the range of micro-perforated plate, while the hole diameter of PB 2 is very large. For PB 1, Maa's model and Beranek Ingard's model are used to calculate its surface impedance. The real and imaginary parts of the obtained surface impedance (normalized in logarithmic scale) are compared in Fig. 5(a). The comparison shows that the two models agree well with only slight differences, which indicates that Beranek Ingard's model can be used to model the micro-perforated plate. For PB 2 with larger holes, Allard Ingard's model and Beranek Ingard's model are used to calculate its surface impedance. The real and the imaginary part of the results are plotted in Fig. 5(b). An excellent agreement is observed, suggesting that Beranek Ingard's model can also be used to model a PB with large hole diameters. Therefore, Beranek Ingard's model is selected as the

modeling tool for the PB hereafter, which simplifies the procedure when switching between small hole and large hole models is needed.

	t(mm)	δ	R_h(mm)
PB 1	0.2	1%	0.5
PB 2	0.2	1%	10

Table 1: Parameters for the tested PB configurations.

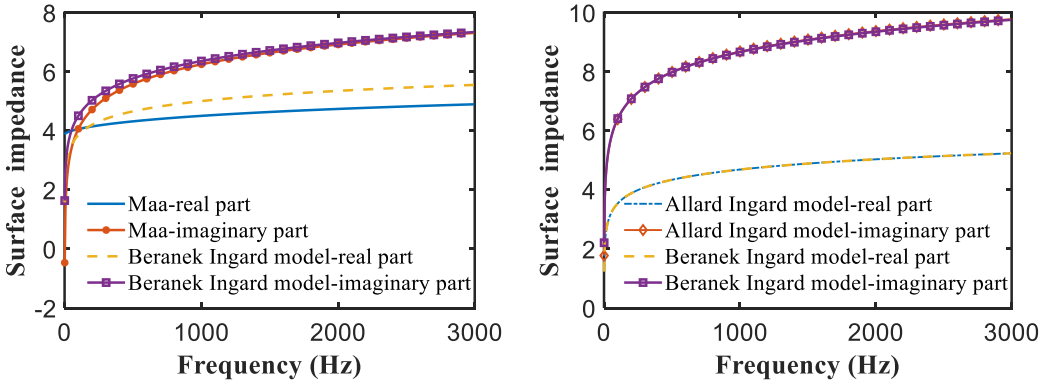

(a) (b)

Fig. 5. Surface impedance comparison of different PB configurations (a) PB 1 (b) PB 2.

After determining the suitable model for the PB, the validity of the plane wave and lumped volume models for the backing cavity, as described in Eq. 14 and Eq. 17, respectively, needs to be verified. Furthermore, the effectiveness and the accuracy of the TMM modeling for the SBH-PB structure is also verified. Numerical simulations are carried out to calculate the reflection coefficients of different SBH-PB configurations. The TMM predictions are compared with those obtained from FEM analysis [30], such that the accuracy of the TMM can be verified. Two SBH-PB structures are considered here, whose constituting parameters are given in Table. 2. Each SBH-PB structure is discretized into 40 segments ($N = 40$) with equal widths, such that the length of each discretized element is 2.5 mm. The inner radius of the rings is assumed to follow a linear decay function as:

$$h(x) = \frac{r - R}{L}x + r \tag{29}$$

where x is the position along the waveguide direction, $-100\ \text{mm} < x < 0$. Same as before, the validation is conducted based on these two cases with different hole diameters R_h, where configuration 1 has a small hole diameter of the PB and configuration 2 has a large hole diameter of the PB. The geometric layout of the SBH structure, t and δ of the PB are kept the same for both cases. For the FEM simulation, commercial software COMSOL Multiphysics is used. Incident plane wave is used, and the duct is filled with air with $\rho_0 = 1.215\ \text{kg/m}^3$ and $c_0 = 340$ m/s. The damping loss in the SBH-PB region is considered by using a complex sound speed $c_0 = 340(1 + 0.05j)$ m/s.

Table 2: Parameters for the tested SBH-PB configurations.

	R(mm)	r(mm)	L(mm)	d(mm)	t(mm)	δ	R_h(mm)
Configuration 1	30	3	100	2.5	0.2	1%	0.5
Configuration 2	30	3	100	2.5	0.2	1%	10

The reflection coefficients at the entrance of the SBH-PB structures are calculated using TMM, which are compared with those obtained by FEM. In the TMM calculation, the two previously discussed modeling methods for the backing cavity are tested. The results from different TMM models are shown in Fig. 6. The frequency range for calculation is set from 1-3000 Hz, which is lower than the cut-off frequency of the incident duct. The two figures show that the TMM modeling is more accurate when the backing cavity is treated as a lumped volume, evidenced by a better agreement with the FEM results. The TMM with lumped volume treatment for the backing cavity agrees well with numerical results in terms of general trend and magnitude for both hole diameters, demonstrating that TMM is accurate to predict the reflection coefficient of the SBH-PB structure regardless of the hole size. Hence, TMM with lumped volume treatment for the backing cavity and Beranek Ingard's model for the surface impedance of PB will be used in the parametric studies and numerical analyses hereafter.

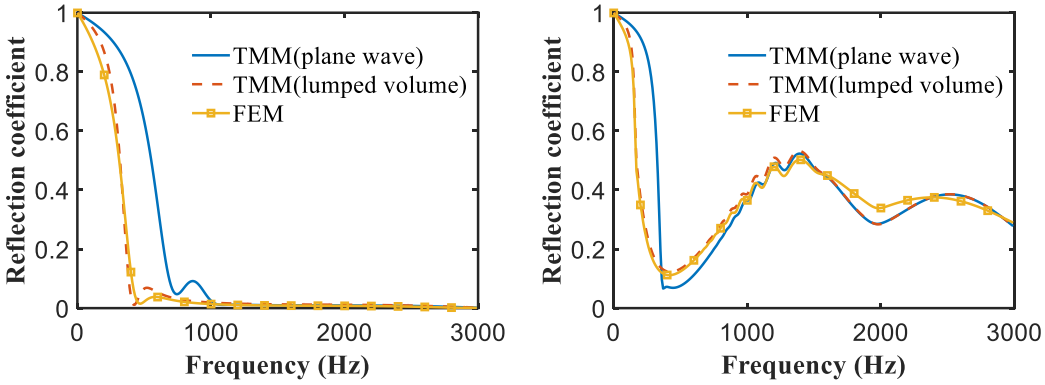

Fig. 6. Reflection coefficients of the closed-end SBH-PB with different hole diameters and different methods (a) R_h =0.5 mm (b) R_h =10 mm. The plate thickness t and perforation ratio δ are kept the same.

3.2 Advantages of embedding PB

By combining conventional SBH and PB into an integrated structure, this section discusses the advantages of the SBH-PB over the original form of SBH, in terms of improving the accuracy of the TMM, enhancing sound absorption performance, and reducing the number of rings required for achieving notable SBH effects. In this regard, we perform investigations for cases with and without PB.

3.2.1 Improving the accuracy of the TMM

In Section 3.1, it is verified that TMM modeling for the SBH-PB structure is accurate. Similarly, for the same duct without PB, TMM prediction is compared to the numerical simulation from FEM. The SBH has the same geometric parameters as the SBH-PB in Fig. 6, but with PB removed. The reflection coefficients obtained by the TMM and FEM are compared in Fig. 7. Comparisons between Fig. 6 and Fig. 7 show that the TMM results agree much better with the FEM results for the SBH-PB. The TMM results for the SBH structure alone are higher than expected, with rather large discrepancies at high frequencies. To investigate the reasons, the sound pressure distribution in the SBH and that in the SBH-PB (R_h = 0.5 mm, the same model of configuration 1) ducts at 2481 Hz are calculated by FEM, with results plotted in Fig. 8 for comparison. At this frequency, the calculated

reflection coefficients using TMM and FEM match very well for the SBH-PB, but differ significantly for the SBH alone. The left pressure distribution figure shows that in the SBH structure without PB, the sound interaction between the shrinking duct and the backing air cavities is strong, especially over their connecting regions. Within the span of the neck regions, pressure fluctuations can be clearly observed (within the boxed area in the figure), indicating that the acoustic interaction between the backing air cavities is also very strong. Furthermore, uneven sound pressure distribution in the inner duct of each discretized layer is obvious, suggesting that the plane wave assumption in the TMM modeling may no longer be valid. Figure 8 further shows the sound pressure distribution along the interface between the backing cavity and the inner duct, for cases without and with PB, respectively. It can be seen that the sound pressure distribution is a continuous curve for the case without PB, which means that three-dimensional effect is significant at the neck region of each discretized layer. The TMM modeling, which assumes only plane-waves, thus cannot capture the pressure variation and leads to significant errors. While for the case with PB, the sound pressure distribution becomes a discontinuous but discrete line. The three-dimensional effect is weakened such that the coupling between the inner and outer ducts can be described with a one-dimensional quantity, conducive to the application of TMM modeling. Since TMM modeling assumes the connecting regions to be in a point-to-point-like simple relation which neglects the pressure variations in the neck area and the interactions among the cavities, it is incapable of capturing the three-dimensional effect and higher-order propagation modes in the SBH. In contrast, the accuracy of the TMM prediction is greatly improved for the SBH-PB structure, owing to the weakened interaction and constraint propagating modes at the connecting areas by the added PB. Overall, the TMM is more suitable to model SBH with the inclusion of perforated boundary, where the validity of the plane wave assumption in the analytical modeling is better guaranteed.

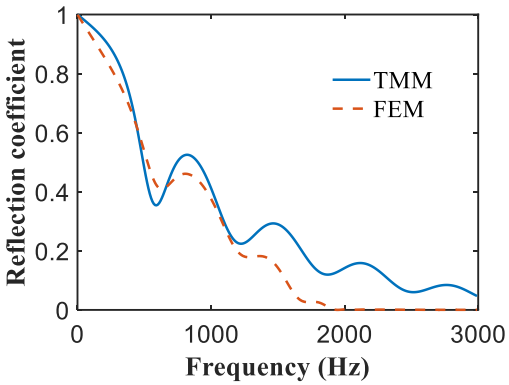

Fig. 7. Reflection coefficients of closed-end SBH calculated using TMM and FEM show large discrepancies.

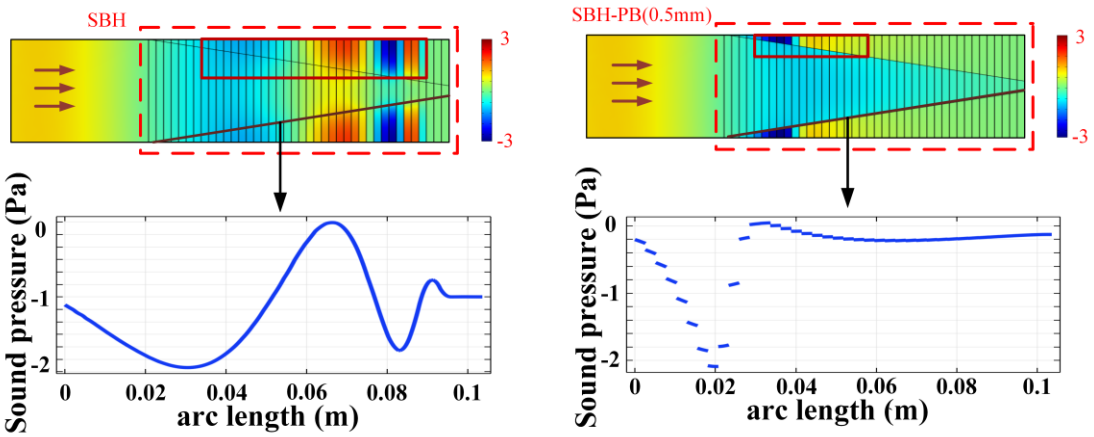

Fig. 8. Sound pressure distribution in the duct with SBH or SBH-PB (hole diameter R_h =0.5 mm) at 2481 Hz and the sound pressure distributions along the line at the interface between the backing cavity and the inner duct.

3.2.2 Enhanced sound absorption performance

In the SBH-PB structure, a perforated boundary is added to increase the energy dissipation, which is expected to provide a much higher damping as compared to the intrinsic air damping in the SBH alone. It is however unknown by how much the sound absorption coefficient can be improved, and whether the introduction of the PB will affect the slow-wave phenomenon. To verify these, we compare the sound absorption performance of the SBH and that of the SBH-PB in this section. The effect of adding PB on the slow wave effect will be discussed in the next section. The geometric parameters of the SBH remain the same as those used in the previous section. The hole diameter of the PB is chosen as $R_h = 0.2$ mm and the perforation ratio $\delta = 1\%$, to be consistent with the samples tested in the experiment. The parameters of the SBH and the SBH-PB are given in Table 3.

	R(mm)	r(mm)	L(mm)	d(mm)	t(mm)	δ	R_h(mm)
SBH	30	3	100	2.5	—	—	—
SBH-PB	30	3	100	2.5	0.2	1%	0.2

Table 3: Parameters for the tested SBH and SBH-PB.

The sound absorption coefficients of the SBH and SBH-PB are calculated and compared in Fig. 9. The figure shows that the absorption coefficient of the SBH-PB is much higher than that of the SBH over the entire frequency band. The improvement is more significant above 500Hz, where the average sound absorption coefficient of SBH-PB is close to one. The sound absorption performance of the SBH is therefore greatly improved through adding PB, which can be used as an effective sound absorbing device.

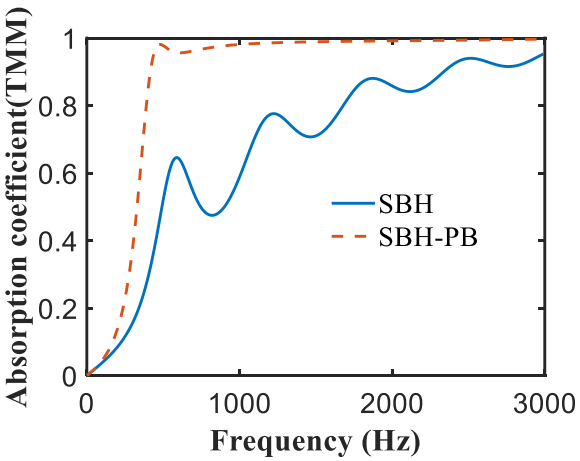

Fig. 9. Absorption coefficients of the selected SBH and SBH-PB.

3.2.3 Number of required rings

It was described in the original theoretical framework of SBH that, in order to generate a consistent and meaningful slow-sound effect, a smooth and gradual impedance variation along the side boundary of the inner duct is required. This typically requires SBH to be constructed with a large number of rings, as discussed in previous studies [18]. However, such requirement is practically unrealistic and extremely challenging in terms of fabrication and engineering application. To understand whether the addition of the PB can eventually alleviate this problem, TMM simulation is performed to calculate the absorption coefficient of the SBH and the SBH-PB with different ring numbers, as presented in Fig. 10(a) and Fig. 10(b), respectively. The number of discretized layers for the SBH and the SBH-PB is chosen as 40, 20, 7, 4, corresponding to the cases with 39, 19, 6 and 3 rings, respectively. Other parameters of the SBH and the SBH-PB remain the same as those tabulated in Table 3. Figure 10(a) shows that SBH-PB structure, with 7 to 39 rings, offers basically the same absorption coefficients, which stabilizes at one above 500Hz. When the ring number is reduced to 3, the curve slightly drops, but the average sound absorption above 1000 Hz is still above 0.8. Figure 10(b) shows that the SBH would need more than 19 rings to achieve similar performance. Furthermore, the SBH needs more than 19 rings to achieve a performance comparable to the SBH-PB with only 4 rings. Therefore, from the perspective of sound absorber design, the SBH-PB requires fewer rings than the SBH, which facilitates the practical application in the design of noise reduction devices.

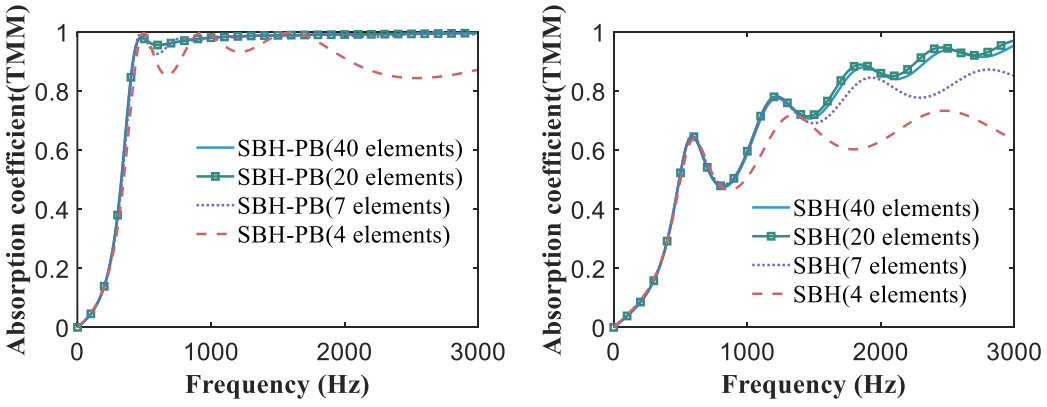

(a) (b)

Fig. 10. Absorption coefficients of the SBH-PB and SBH with different ring number (a) the SBH-

PB (b) the SBH.

3.3 Impedance tube experiment

The first experiment is to validate the accuracy of the TMM prediction in terms of sound absorption of the SBH-PB. This experiment was performed in a standard impedance tube, using the standard two-microphone transfer function method to obtain the absorption coefficient of the tested model. The detailed set-up and results of this experiment are described in the following. A test sample has been designed and manufactured, and its inner diameter at the beginning end is close to that of the impedance tube and it has a length within the allowable installation area. The tested SBH-PB model has the same set of parameters as Table 4. From the Fig. 10, it can be seen that the results are already good enough when the structure contains only 7 elements, thus a SBH with 7 segments was manufactured. The SBH-PB contains 6 rings of 2 mm thick each and the radius of the inner rings is also assumed to follow the liner decay function as before. The lined PB, made of aluminum, was embedded into the SBH between the rings. The prototype was manufactured by firstly dividing the whole structure into 7 sections according to different elements. Each section consists of a PB and a backing cavity. The backing cavities were 3D printed by using ABS resin. All these sections were assembled using glue to form the final prototype. The SBH-PB model was installed at one end of the impedance tube. Two microphones which were mounted in the tube measure and separate the incident and reflected sound waves, as shown in Fig. 11. The specific test rig settings for sound absorption measurement can be found in [30], and the related details are not repeated here. The measured absorption coefficient of the tested SBH-PB is displayed in Fig. 12, alongside the calculated ones by TMM and FEM. Comparing the measured and predicted results shows good agreement among the three curves in terms of general trend and magnitude, indicating that TMM is accurate enough to predict the sound absorption coefficient of the SBH-PB. However, subtle differences exist between the measured and TMM results at low frequencies. This may be attributed to the slight error caused by Beranek Ingard's model for calculating the surface impedance of PB with too small hole diameter. Nevertheless, the figure shows that the absorption coefficient of the SBH-PB remains above 0.9 after 300 Hz, which implies this structure offers persistent high sound absorption at high frequencies as well as the broadband feature for sound absorption. The SBH-PB can then be used as a broadband and high-efficiency sound-absorbing device.

	R(mm)	r(mm)	L(mm)	t(mm)	δ	R_h(mm)
SBH-PB	49	1.5	180	0.2	1%	0.2

Table 4: Parameters for the tested SBH-PB.

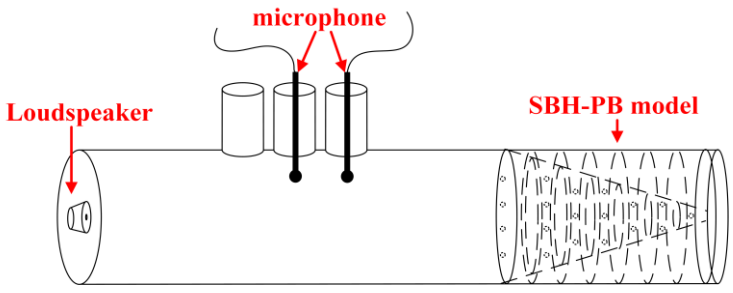

Fig. 11. Schematic of the experimental layout in the impedance tube.

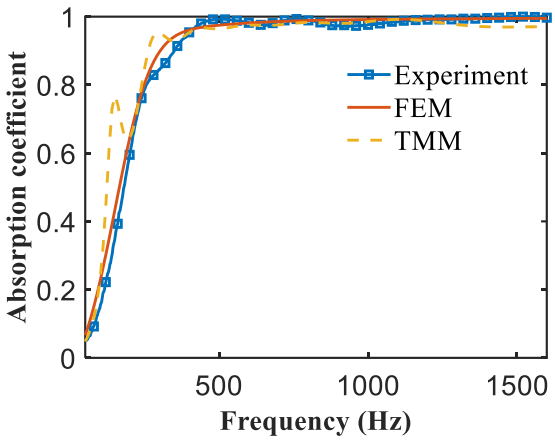

Fig. 12. Absorption coefficient of the SBH-PB measured by the experimental method and its comparison with TMM and FEM result.

4. Slow-wave phenomenon: Transient simulations and time-domain experiment

In the previous section, the accuracy of the TMM has been verified and the acoustic characteristics of the proposed SBH-PB structure in the frequency domain have been analyzed. This section further investigates the slow-wave phenomenon in the time domain, with a view of providing more physical insights into the SBH phenomena.

4.1 Transient simulations

To elucidate how the introduction of PB might affect the slow-wave phenomenon, time domain analyses are conducted in this Section, with corresponding experiments to be discussed later. Transient simulations using COMSOL are performed on the cases with and without PB by tracing the propagation of a wave packet in the SBH structure. Schematics of the geometric models are shown in Fig. 13. The excitation signal is defined as a plane wave at 2000 Hz. In order to reduce the influence of reflected waves, the termination of the SBH end is extended, which is connected to a duct with non-reflecting boundary condition to allow outgoing waves to propagate without reflections. By tracing the propagation of wavefront along the duct at different time instants t_1 and t_2, the equivalent sound speed can be derived. The oscillographs of wave packets at different time instants along the center axis of the duct are all presented in Fig. 14(a) and Fig. 14(b), for the case of SBH and SBH-PB, respectively. The SBH segments in both figures are located between distance 0.3 m and 0.4 m. Distance below 0.3 m represents the incident duct, and above 0.4 m represents the outgoing small duct. The sound propagation speed can be deduced by tracing the position and time arrivals of the first peak. These two curves are drawn together to obtain Fig. 14(c), in which the slopes of the curves indicate the sound propagation speed. Notably, the black line in Fig. 14(c) represents the case where there is no retarding structure in the duct, with a slope being a constant of 340 m/s, which equals to the sound speed in air. The slopes of both SBH and SBH-PB curves show a gradually decreasing trend in the section corresponding to the retarding structure, which indicates a reduced speed of the sound, evidencing the expected slow-wave phenomenon. It is also found that the blue line with rectangle markers (corresponding to the SBH) declines slightly faster than the red line with diamond makers (corresponding to the SBH-PB), which means that the original SBH exerts slightly stronger slow-wave effect, and the traveling time of sound waves to pass through its

region is slightly longer. Overall, when PB is added to the SBH, its adverse influence on the slow-wave effect is very minor, such that the basic features of the slow-sound are retained. Nonetheless, the addition of the PB increases the energy dissipation of the structure, which greatly improves the sound absorption coefficient. Therefore, by combining the slow-sound effect in the SBH and the energy dissipation in the perforation, the overall black hole effect is maintained and the acoustic performance of SBH-PB is much better than that of the original SBH, making this new structure a better design for sound absorption applications.

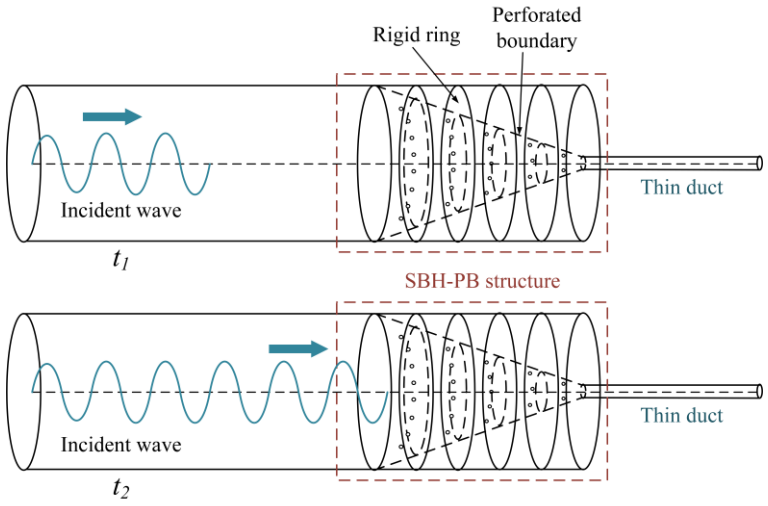

Fig. 13. Schematic of the SBH-PB model used in time-domain simulations and propagation of incident wave along the center axis of the duct at different times $t_1$and t_2.

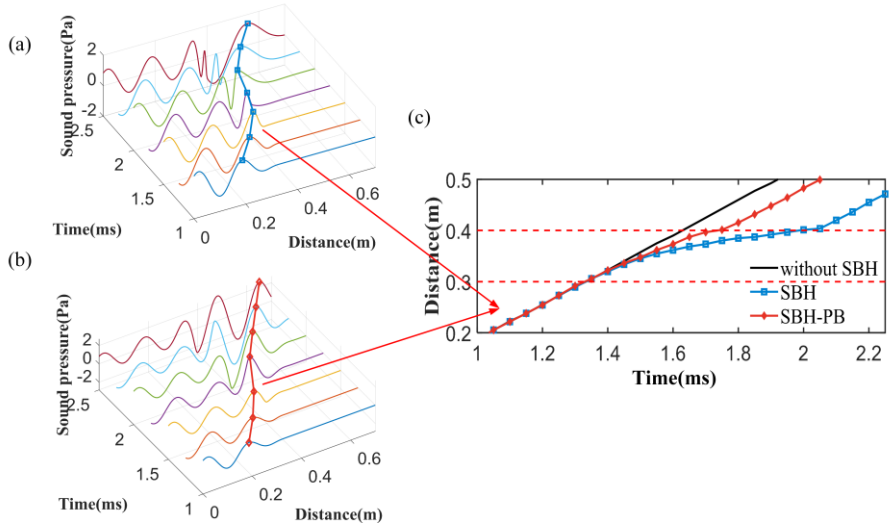

Fig. 14. Oscillographs of wave packets at different times in the duct with (a) the SBH (b) the SBH-PB, (c) the comparison of propagation distance curves of first peak between SBH and SBH-PB.

In section 3.2.3, it was discussed that the addition of PB can reduce the required number of inner rings. Whether the slow-wave effect is affected by fewer rings is further analyzed in the time domain. Transient simulations are again performed for the cases with/without PB and with different number of rings. The models are the same as those used in Fig. 10. By the same token, the arrival times and positions of the first peak signal are traced, for the same 2000 Hz plane wave excitation. The propagation diagrams of the wavefront versus time, whose slope informs on the resultant sound

speed, are presented in Fig. 15. The sound speed variations in the SBH and SBH-PB with different ring numbers can be observed from Figs. 15(a) and (b), respectively. It can be seen from Fig.15(a) that the effect of ring numbers on the SBH-PB is small. With only 3 rings, the wave speed reduction effect is similar to the case with more rings. Figure 15(b) shows that for the SBH without PB, the slow wave effect is adversely affected by the reduced ring number, implying that a sufficient number of rings is required for SBH. From the perspective of the slow wave phenomenon, adding PB into the SBH structure also alleviates the stringent requirement on the number of rings.

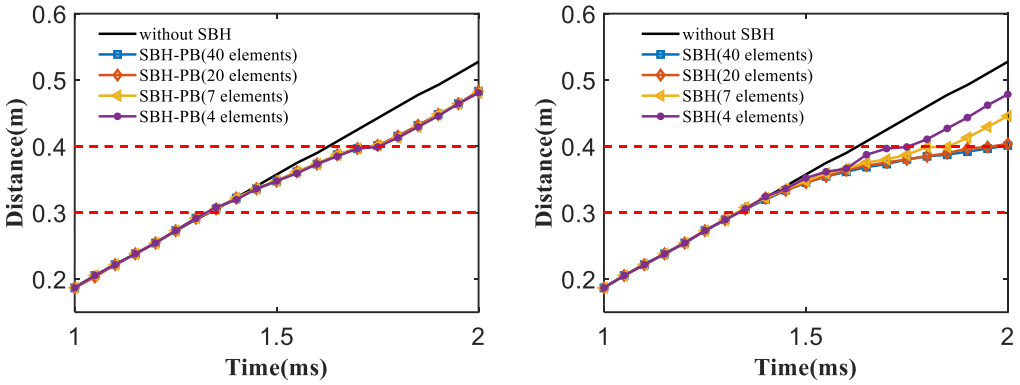

Fig. 15. Propagation distance curve of the first peak of the sound wave at 2000 Hz (a) the SBH-PB (b) the SBH.

4.2 Time domain experiment for slow-wave visualization and confirmation

To experimentally demonstrate the slow wave phenomenon and quantify the reduction of sound speed, an acoustic duct system was customized to measure the evolution of a wave packet along its propagation path. This experiment was carried out in a modified impedance tube with customized ability to measure the temporal response of acoustic signals. A movable microphone was used to capture the temporal signals at various positions along the duct, and a plot of propagation distance versus time is recorded to show the change of the wave speed along the wave propagation. The experimental set-up is shown in Fig. 16, where the SBH/SBH-PB structure is placed in the impedance tube, which is connected to an open duct with a length of 130 mm to allow free transmissions. The experimental system as shown in Fig. 16(b) replicates the transient simulation models as described in Fig. 13. The SBH and SBH-PB prototypes have the same geometric parameters as those used in the previous frequency-domain experiment (Table. 4). Specific sections of the duct systems are shown in Figs. 16(a), (b), (c) and (d), respectively. A tone burst excitation signal (five-cycle tone burst excitation windowed by the Hann function) was produced by the signal generator, which was then enhanced by a power amplifier to drive a loudspeaker at the entrance of the duct. Considering the small internal space inside the SBH-PB, a MEMS microphone was used. The microphone was attached to a slender rod and placed on a support as shown in Figs. 16(b) and (c), so that it could move freely to different positions. Another MEMS microphone was fix-attached to the end of the thin tube. As shown in Fig. 16(e), we selected 7 positions to measure the temporal response, including two positions before the SBH area, four positions in the SBH area, and one in the outgoing duct. The oscillographs of wave packets at different positions were then constructed. The sound propagation in the SBH and SBH-PB are plotted in Figs. 17(a) and (b), respectively, with the slope of the curves being calculated to indicate

the sound speed. The violet solid line first represents the case without retarding structure in the duct, whose slope is consistently at 340 m/s. The decline of propagation curves and the reduction of the slope for both cases with SBH and SBH-PB indeed show the slow wave effect, and the experimentally measured results agree well with the simulated ones by the transient FEM analyses. The time duration for the wavefront to travel through the SBH structure is at least two times longer than the case with the empty duct. After the SBH section, the sound propagation speed reverts back to the original speed of 340 m/s. The time domain simulation provides an accurate tool for analyzing the transient propagation of sound wave and it can be used to study the slow-wave phenomenon of the SBH. The alight discrepancies may be attributed to a few plausible reasons, including the accuracy in terms of placement of the moving MEMS microphone, inaccurate positioning, time delay in the measurement systems, and so on. Overall, the simulation findings are well supported by the experimental measurements, and the SBH-specific slow-sound phenomenon is clearly visualized, probably for the first time, in the time-domain.

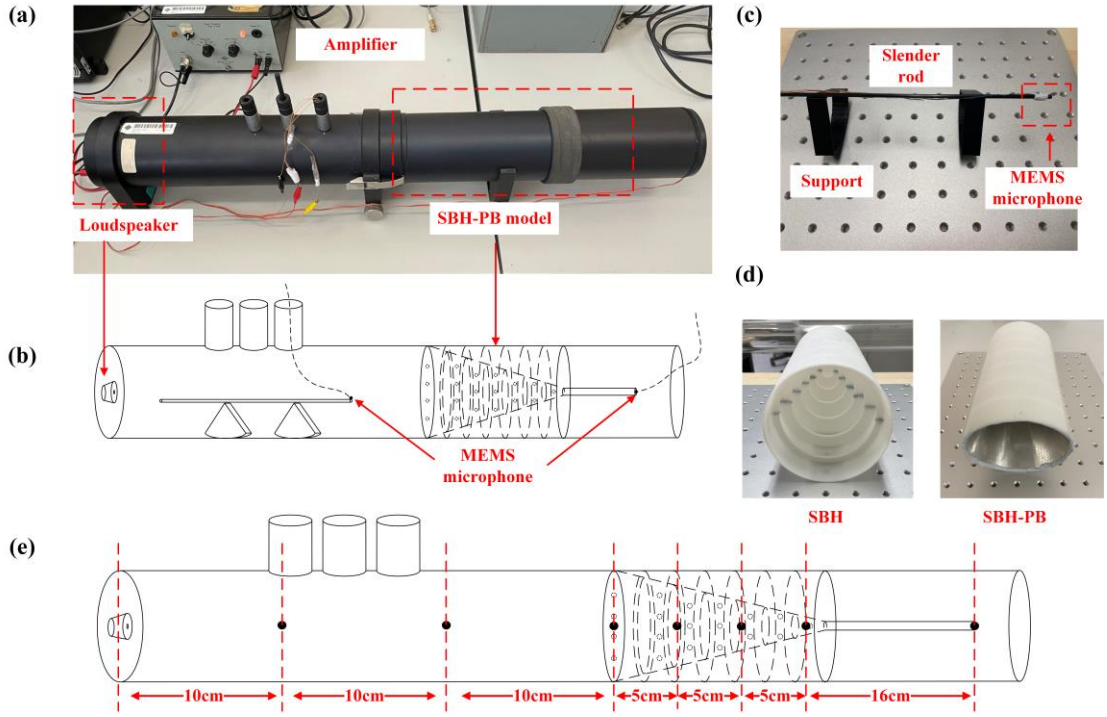

Fig. 16. (a) Photograph of the experimental layout, (b) schematic of the experimental layout, (c) the movable MEMS microphone in the duct, (d) the test prototypes and (e) schematic of the measured positions.

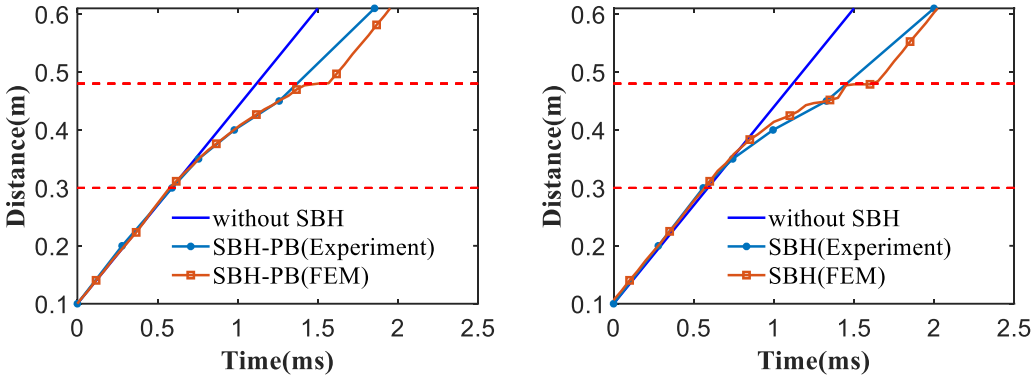

(a) (b)

Fig. 17. Time-varying propagation distance curve of the second peak of the sound wave (a) the SBH-PB (b) the SBH.

4.3 SBH with and without PB

Finally, experiments were conducted on SBH structures with and without PB to conclude the predicted improvement of sound absorption performance and the effect on the slow-sound effect. The impedance tube experiment was conducted again for a bare SBH without PB. The measured sound absorption coefficient, as described in section 3.3, is compared with the SBH-PB results as shown in Fig. 18. The measurement frequency range is from 50 Hz to 1600 Hz. It can be seen that the absorption coefficient of the SBH-PB is much higher than that of the SBH over the entire frequency range. After 600 Hz, the absorption coefficient of the SBH-PB stabilizes at almost at 1, while that of the SBH is only around 0.5. The SBH-PB therefore quite obviously outperforms the original SBH, and the observed trend is in good agreement with the simulations discussed in Fig. 9.

As for the slow wave effect in the time domain, a similar comparison of the SBH and the SBH-PB is also conducted. The curves showing the propagation distance versus time are compared in Fig. 19. As previously seen from the simulation findings, the sound speed reduction is slightly stronger in the SBH without PB, and experimental results verify this trend. It is therefore clear that the improved sound absorption performance of the SBH-PB is attributed to the increased energy dissipation effect owing to the added perforations, not necessarily to the slow-sound effect itself. To design optimal slow-sound absorber that exhibits both strong wave retarding effect and broadband sound absorption, the slow-sound and energy dissipation effects need to be balanced through design trade-offs. The addition of the PB as proposed and analyzed in this work provides a feasible means to achieve different design targets.

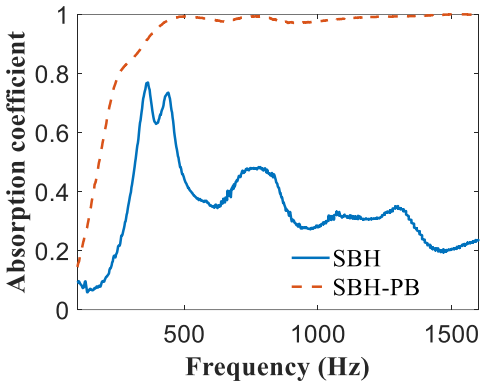

Fig. 18. Comparison of the sound absorption coefficient between the SBH and the SBH-PB.

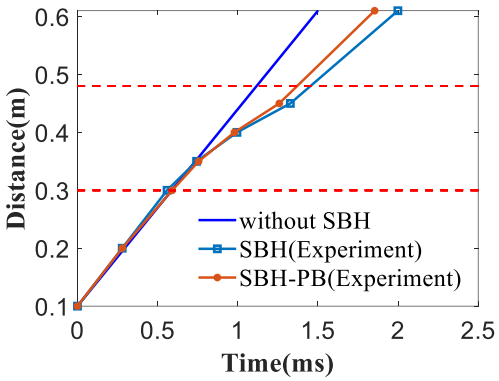

Fig. 19. Comparison of the time-varying propagation distance curve of the second peak between the SBH and the SBH-PB.

5. Conclusions

In summary, a SBH structure with embedded perforated boundary is investigated in this study, and a TMM model is developed for its modeling and analyses. The validity of the TMM in the presence of the PB is verified through comparisons with numerical results using FEM, which is later also confirmed by experiment. The advantages of adding PB to the original SBH structure are explained from three aspects based on TMM results: 1) The addition of the PB allows for increased accuracy of the TMM prediction due to the weakened three-dimensional effect such that acoustic interactions are confined in the directions normal to the PB through perforated holes; 2) the overall sound absorption performance of the SBH is improved by the deployment of the PB, as a result of the increased micro-perforation dissipation; and 3) the proposed SBH-PB structure requires a smaller number of inner rings than the original form of SBH to achieve the expected SBH effects, which facilitates the structural design and implementation. The effectiveness and accuracy of the TMM modeling are verified by impedance tube experiment in terms of the measured sound absorption coefficient, which also demonstrates the superiority of the proposed SBH-PB structure. The slow-wave phenomenon is observed and quantified through transient simulations in the time domain. A significant reduction of the sound propagation speed is observed by tracking the wave packets passing through the SBH portion inside a duct. Experimentally, the evolution of sound propagation process is measured and confirmed using a customized acoustic duct, in which the reduction of sound speed is captured by tracking the arrival time of the tone-burst signals. The time-

domain experiments agree well with the transient simulations, which confirms the occurrence of the slow-sound effect and visualizes its gradually varying spatial distribution. These findings are believed to be of significant value for future research on slow-sound devices and design of SBH-based sound absorbers.

Declaration of Competing Interest

The authors declare that they have no known competing financial interests or personal relationships that could have appeared to influence the work reported in this paper.

Acknowledgements

This research is supported by Research Grants Council of Hong Kong under grant No. PolyU 15201822. Yu Xiang acknowledges the start-up funding support from the Department of Mechanical Engineering and the Hong Kong Polytechnic University.

Reference

[1] V.V. Krylov, Acoustic black holes: recent developments in the theory and applications, IEEE T. Ultrason. Ferr. 61 (2014) 1296-1306. https://doi.org/10.1109/TUFFC.2014.3036.

[2] A. Pelat, F. Gautier, S.C. Conlon, F. Semperlotti, The acoustic black hole: A review of theory and applications, J. Sound Vib. 476 (2020) 115316. https://doi.org/10.1016/j.jsv.2020.115316.

[3] C. Pekeris, Theory of propagation of sound in a half-space of variable sound velocity under conditions of formation of a shadow zone, J. Acoust. Soc. Am. 18 (1946) 295-315. https://doi.org/10.1121/1.1916366.

[4] M. Mironov, Propagation of a flexural wave in a plate whose thickness decreases smoothly to zero in a finite interval, Sov. Phys. Acoust+ 34 (1988) 318-319.

[5] V. Krylov, A. Shuvalov, Propagation of lo-calised flexural vibrations along plate edges described by a power law, IOA 22 (2000) 263-270.

[6] V.V. Krylov, Localized acoustic modes of a quadratic solid wedge, Mosc. U. Phys. B+ 45 (1990) 65-69.

[7] V. Denis, F. Gautier, A. Pelat, J. Poittevin, Measurement and modelling of the reflection coefficient of an acoustic black hole termination, J. Sound Vib. 349 (2015) 67-79. https://doi.org/10.1016/j.jsv.2015.03.043.

[8] N. Gao, Z. Wei, H. Hou, A.O. Krushynska, Design and experimental investigation of V-folded beams with acoustic black hole indentations, J. Acoust. Soc. Am. 145 (2019) EL79-EL83. https://doi.org/10.1121/1.5088027.

[9] T. Zhou, J.-D. Chazot, E. Perrey-Debain, L. Cheng, Partition of unity finite element method for the modelling of acoustic black hole wedges, J. Sound Vib. 475 (2020) 115266. https://doi.org/10.1016/j.jsv.2020.115266.

[10] V.V. Krylov, Geometrical-acoustics approach to the description of localized vibrational modes of an elastic solid wedge, Sov. Phys. Tech. Phys. 35 (1990) 137-140.

[11] X. Li, Q. Ding, Sound radiation of a beam with a wedge-shaped edge embedding acoustic black hole feature, J. Sound Vib. 439 (2019) 287-299. https://doi.org/10.1016/j.jsv.2018.10.009.

[12] J. Deng, L. Zheng, O. Guasch, H. Wu, P. Zeng, Y. Zuo, Gaussian expansion for the vibration analysis of plates with multiple acoustic black holes indentations, Mech. Syst. Signal Pr. 131 (2019) 317-334.

https://doi.org/10.1016/j.ymssp.2019.05.024.
[13] L. Tang, L. Cheng, H. Ji, J. Qiu, Characterization of acoustic black hole effect using a one-dimensional fully-coupled and wavelet-decomposed semi-analytical model, J. Sound Vib. 374 (2016) 172-184. https://doi.org/10.1016/j.jsv.2016.03.031.
[14] Y. Zhang, K. Chen, Y. Cheng, Z. Wei, Lightweight-high-stiffness vibration insulator with ultra-broad band using graded double-leaf acoustic black holes, Appl. Phys. Express 13 (2020) 017007. https://doi.org/10.7567/1882-0786/ab6411.
[15] S.S. Ganti, T.-W. Liu, F. Semperlotti, Topological edge states in phononic plates with embedded acoustic black holes, J. Sound Vib. 466 (2020) 115060. https://doi.org/10.1016/j.jsv.2019.115060.
[16] D. O'Boy, V.V. Krylov, V. Kralovic, Damping of flexural vibrations in rectangular plates using the acoustic black hole effect, J. Sound Vib. 329 (2010) 4672-4688. https://doi.org/10.1016/j.jsv.2010.05.019.
[17] L. Zhao, S.C. Conlon, F. Semperlotti, Broadband energy harvesting using acoustic black hole structural tailoring, Smart Mater. Struct. 23 (2014) 065021. https://doi.org/10.1088/0964-1726/23/6/065021.
[18] M. Mironov, V. Pislyakov, One-dimensional acoustic waves in retarding structures with propagation velocity tending to zero, Acoust. Phys+ 48 (2002) 347-352. https://doi.org/10.1134/1.1478121.
[19] A. Mousavi, M. Berggren, E. Wadbro, How the waveguide acoustic black hole works: A study of possible damping mechanisms, J. Acoust. Soc. Am. 151 (2022) 4279-4290. https://doi.org/10.1121/10.0011788.
[20] N. Sharma, O. Umnova, A. Moorhouse, Low frequency sound absorption through a muffler with metamaterial lining, in: 24th ICSV, LND, 2017.
[21] O. Guasch, M. Arnela, P. Sánchez-Martín, Transfer matrices to characterize linear and quadratic acoustic black holes in duct terminations, J. Sound Vib. 395 (2017) 65-79. https://doi.org/10.1016/j.jsv.2017.02.007.
[22] J.P. Hollkamp, F. Semperlotti, Application of fractional order operators to the simulation of ducts with acoustic black hole terminations, J. Sound Vib. 465 (2020) 115035. https://doi.org/10.1016/j.jsv.2019.115035.
[23] Y. Mi, W. Zhai, L. Cheng, C. Xi, X. Yu, Wave trapping by acoustic black hole: Simultaneous reduction of sound reflection and transmission, Appl. Phys. Lett. 118 (2021) 114101. https://doi.org/10.1063/5.0042514.
[24] A.A.E. Ouahabi, V.V. Krylov, D. O'Boy, Investigation of the acoustic black hole termination for sound waves propagating in cylindrical waveguides, in: InterNoise 2015, 2015. https://hdl.handle.net/2134/18926.
[25] M. Deaconu, D. Radulescu, G. Vizitiu, Acoustic study of different mufflers based on metamaterials using the black hole principle for aircraft industry, in: Euronoise, 2018, pp. 2271-2275.
[26] Y. Mi, L. Cheng, W. Zhai, X. Yu, Broadband low-frequency sound attenuation in duct with embedded periodic sonic black holes, J. Sound Vib. 536 (2022) 117138. https://doi.org/10.1016/j.jsv.2022.117138.
[27] M. Mironov, V. Pislyakov, One-dimensional sonic black holes: Exact analytical solution and experiments, J. Sound Vib. 473 (2020) 115223. https://doi.org/10.1016/j.jsv.2020.115223.
[28] N. Sharma, O. Umnova, Study of sound absorption capability of silencers based on the acoustic black hole effect, in: ISMA2018, 2018, pp. 1121-1126.
[29] J.W. Chua, X. Li, X. Yu, W. Zhai, Novel slow-sound lattice absorbers based on the sonic black hole, Compos. Struct. (2022) 116434. https://doi.org/10.1016/j.compstruct.2022.116434.

[30] X. Zhang, L. Cheng, Broadband and low frequency sound absorption by Sonic black holes with Micro-perforated boundaries, J. Sound Vib. 512 (2021) 116401. https://doi.org/10.1016/j.jsv.2021.116401.
[31] D.-Y. Maa, Potential of microperforated panel absorber, J. Acoust. Soc. Am. 104 (1998) 2861-2866. https://doi.org/10.1121/1.423870.
[32] N. Atalla, F. Sgard, Modeling of perforated plates and screens using rigid frame porous models, J. Sound Vib. 303 (2007) 195-208. https://doi.org/10.1016/j.jsv.2007.01.012.